


Electronic interferometry with ultrashort plasmonic pulses

Received: 29 December 2024

Accepted: 3 April 2025

Published online: 19 May 2025

 Check for updates

Seddik Ouacel ¹, Lucas Mazzella ¹, Thomas Kloss ¹, Matteo Aluffi ¹, Thomas Vasselon ¹, Hermann Edlbauer ¹, Junliang Wang ¹, Clément Geffroy ¹, Jashwanth Shaju¹, Arne Ludwig ², Andreas D. Wieck ², Michihisa Yamamoto ^{3,4}, David Pomaranski⁴, Shintaro Takada ^{5,6,7}, Nobu-Hisa Kaneko ⁸, Giorgos Georgiou ⁹, Xavier Waintal ¹⁰, Matias Urdampilleta ¹, Hermann Sellier ¹ & Christopher Bäuerle ¹ ✉

Electronic flying qubits offer an interesting alternative to photonic qubits: electrons propagate slower, hence easier to control in real time, and Coulomb interaction enables direct entanglement between different qubits. Although their coherence time is limited, flying electrons in the form of picosecond plasmonic pulses could be competitive in terms of the number of achievable coherent operations. The key challenge in achieving this critical milestone is the development of a new technology capable of injecting ‘on-demand’ single-electron wavepackets into quantum devices, with temporal durations comparable to or shorter than the device dimensions. Here, we take a significant step towards achieving this regime in a quantum nanoelectronic system by injecting ultrashort single-electron plasmonic pulses into a 14-micrometer-long Mach-Zehnder interferometer. Our results establish that quantum coherence is robust under the on-demand injection of ultrashort plasmonic pulses, as evidenced by the observation of coherent oscillations in the single-electron regime. Building on this, our results demonstrate the existence of a “non-adiabatic” regime that is prominent at high frequencies. This result highlights the potential of flying qubits as a promising alternative to localised qubit architectures, offering advantages such as a reduced hardware footprint, enhanced connectivity, and scalability for quantum information processing.

Solid-state systems, presently considered for quantum computation, are built from localised two-level systems. Prime examples are superconducting qubits or semiconducting quantum dots^{1,2}. Being localised, they require a fixed amount of hardware per qubit. Conversely, flying

qubits are the only existing quantum technology platform that uses propagating particles. They represent an interesting quantum architecture, as they naturally enable the implementation of quantum interconnects. Currently, flying qubits are associated with photons due

¹Université Grenoble Alpes, CNRS, Grenoble INP, Institut Néel, F-38000 Grenoble, France. ²Lehrstuhl für Angewandte Festkörperphysik, Ruhr-Universität Bochum, Bochum, Germany. ³Center for Emergent Matter Science (CEMS), RIKEN, Saitama, Japan. ⁴Quantum-Phase Electronics Center and Department of Applied Physics, The University of Tokyo, Tokyo, Japan. ⁵Department of Physics, Graduate School of Science, Osaka University, Toyonaka 560-0043, Japan. ⁶Institute for Open and Transdisciplinary Research Initiatives, Osaka University, Suita 560-8531, Japan. ⁷Center for Quantum Information and Quantum Biology (QIQB), Osaka University, Osaka 565-0871, Japan. ⁸National Institute of Advanced Industrial Science and Technology (AIST), National Metrology Institute of Japan (NMIJ), Tsukuba, Ibaraki, Japan. ⁹James Watt School of Engineering, Electronics and Nanoscale Engineering, University of Glasgow, Glasgow G12 8QQ, United Kingdom. ¹⁰Université Grenoble Alpes, CEA, INAC-Phelips, F-38000 Grenoble, France. ✉e-mail: christopher.bauerle@neel.cnrs.fr

to their highly coherent nature, on-demand generation, and inherent scalability³. Photons, however, travel so fast that in-flight dynamical manipulation is impossible, and their trajectories need to be set in advance. Moreover, they do not interact directly with each other, making photon entanglement challenging, and the ‘all-linear’ quantum optics approach⁴ requires post-selection methods. As a result of the very weak photon interaction, a large number of Mach-Zehnder interferometers must be implemented to construct a single two-qubit gate⁵. This inevitably leads to a tremendous increase in hardware overhead.

Despite their much shorter coherence time compared to photons, quantum nanoelectronic circuits have seen enormous progress over the last 10 years. This advancement was driven by the development of on-demand single-electron sources capable of generating single-electron wavepackets with high fidelity^{6–9}. Moreover, Coulomb interactions between two individual co-¹⁰ and counter-propagating electrons^{11,12} have been successfully demonstrated. Such progress marks a significant milestone, paving the way for entanglement of multiple flying electron qubits in the future^{13–15}.

The most convenient method to generate a single-electron excitation is by applying a short voltage pulse to the Ohmic contact of a two-dimensional electron gas (2DEG). This creates a single electron-excitation in the form of a plasmonic pulse¹⁶. Recent experiments have demonstrated the coherent manipulation of single-electron plasmonic pulses in the form of Levitons^{17,18} within a Mach-Zehnder interferometer (MZI) implemented in graphene¹⁹, highlighting their potential for quantum information processing. In addition, their relevance for quantum sensing applications has been demonstrated^{20,21}.

The next milestone towards developing a competitive quantum architecture for flying electron qubits is to reach a regime where the wavepacket’s width is significantly shorter than the quantum device. Such achievement would allow multiple flying qubits to be accommodated within a single quantum processing unit and would enable the implementation of a large number of gate operations during their flight²². Moreover, as the wavepacket width decreases, it inevitably becomes comparable to or shorter than the characteristic timescales of the interferometer. This marks the transition into the non-adiabatic regime where dynamical effects are expected to play an important role²³.

In this work, we demonstrate quantum coherence of ultrashort electron wavepackets in the non-adiabatic regime in an electronic

Mach-Zehnder interferometer. After describing the working principle of the device in the DC regime, we present a detailed characterisation of its nonlinear behavior. This nonlinearity is harnessed to investigate the frequency response of the Mach-Zehnder interferometer via quantum rectification²⁴. Through these measurements, we demonstrate the onset of the non-adiabatic regime for frequencies starting around 1 GHz. Finally, we utilize these findings to establish the presence of non-adiabatic coherent current oscillations driven by ultra-short plasmonic pulses of duration as short as 30 ps.

Results

Electronic Mach-Zehnder interferometer device

The cornerstone of a flying qubit platform is the Mach-Zehnder interferometer (MZI). Here, individual particles are injected on demand, put in a superposition of states at the initial beam splitter, guided through the interferometer, and ultimately, the quantum superposition can be discerned at the two output detectors. Throughout the particle’s trajectory, quantum manipulations can be implemented by electrical gate operations.

In our system, the qubit states are represented by the presence of an electron in the upper $|0\rangle$ or lower $|1\rangle$ arm of the electronic Mach-Zehnder interferometer of a total length of $14\ \mu\text{m}$, as shown in Fig. 1a. To create a superposition between the two states, tunnel-coupled wires (TCW) of a length of $2\ \mu\text{m}$ is employed that acts as an electronic beam splitter. In this device, the electronic waveguides are brought into close proximity, enabling quantum tunneling of the injected wavepackets between them. The tunneling is controlled via the voltage applied to the two tunnel-coupled wires V_{TCW} , providing full electrical control of the beam splitter. The wavepackets are then allowed to propagate through an Aharonov-Bohm ring, where a phase difference between the upper and the lower arm can be induced by varying the magnetic flux ϕ enclosed by the two paths. Alternatively, the phase can be electrically controlled by applying a voltage V_{sg} to the side gates²⁵. A second beam splitter is placed at the end of the ring to enable interference between the two wavepackets, thereby effectively implementing an electronic Mach-Zehnder interferometer^{25,26}.

To investigate the coherent properties of our device, we adopt the following approach. Electrons are injected into the electronic MZI by applying a constant bias voltage V_{dc} to the injection Ohmic contact, as indicated by the left white square in Fig. 1a. The transmitted output

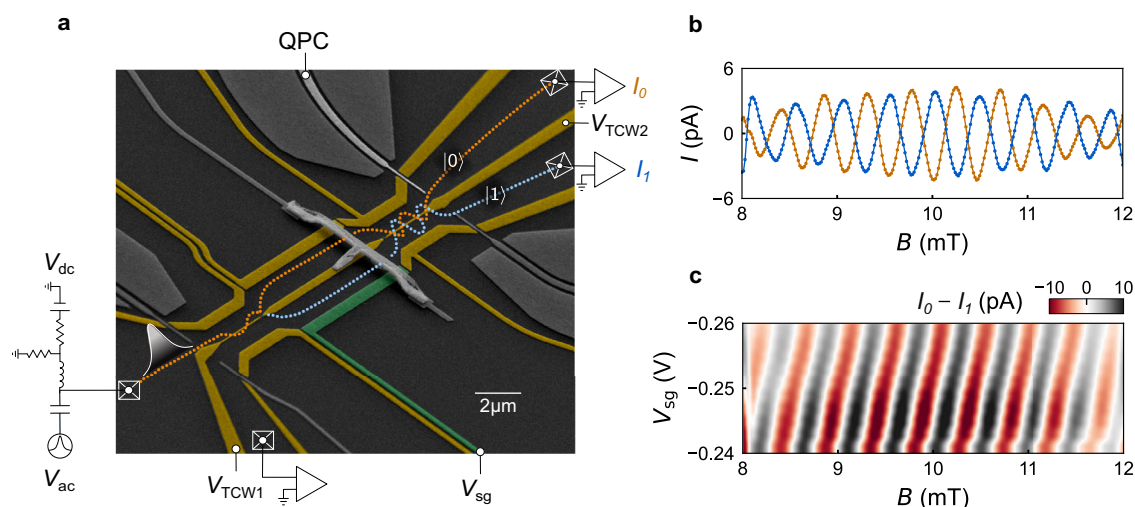


Fig. 1 | Electronic Mach-Zehnder interferometer. **a** Scanning electron micrograph of the electronic Mach-Zehnder interferometer (MZI) device. The electrostatic gates highlighted in color define the electron trajectories indicated by the dotted lines. Electrons are injected into the interferometer through the left Ohmic contact (crossed white square). The output current I_0 (I_1), corresponding to the transmitted

current in the upper (lower) electron waveguide, is measured using a lock-in amplifier. **b** Coherent anti-phase oscillations of the transmitted currents I_0 and I_1 when applying a DC bias where a smooth background has been subtracted. **c**. Coherent oscillations of $I_0 - I_1$ (total oscillating component of the transmitted current) as a function of the magnetic field and the side gate voltage V_{sg} .

currents I_0 and I_1 are then measured as a function of the applied magnetic field B . When the device is properly tuned into a two-path interferometer²⁶, anti-phase oscillations in the currents are observed at the two outputs, as shown in Fig. 1b. Here we plot the oscillating component I where a smooth background current (≈ 1 nA) has been subtracted. We measure a magnetic field periodicity of the current oscillations of $\Delta B = 0.5$ mT, corresponding to a surface area of $S = 8.2 \mu\text{m}^2$, which is consistent with the device geometry. Varying the voltage V_{sg} of the side gate highlighted in green in Fig. 1a, a controlled phase shift between the propagating electrons through the lower arm with respect to the upper one can be achieved. In our case a voltage variation of $\Delta V_{\text{sg}} \approx 20$ mV is sufficient to induce a phase shift of 2π (see Fig. 1c). Demonstrating interference with ultrashort voltage pulses requires a careful understanding of the device's frequency response. When the MZI is driven by a purely sinusoidal signal, the net average current is theoretically expected to be zero. However, as shown in Fig. 3a and c, this is not the case. Instead, we observe current rectification, attributed to a nonlinearity in the device. In the following section, we provide a detailed characterisation of this nonlinearity, which is subsequently utilized to investigate the frequency response of the MZI.

Nonlinearity of the device revealed in DC measurements

We begin by investigating the source of the nonlinearity responsible for the rectification, and thoroughly characterising the device's DC response. Nonlinear effects in mesoscopic transport systems have been studied in the past, with particular focus on quantum point contacts²⁷ and Aharonov-Bohm (AB) rings^{28,29}. In prior research, coherent oscillations in the nonlinear conductance of two-terminal AB rings have been observed, with different proposed origins: in²⁸, the nonlinearity arose from spatial inversion asymmetry while its magnetic field asymmetry was attributed to electron-electron interactions, whereas in²⁹, the nonlinearity was suggested to originate from bias-dependent transmission, though its precise microscopic origin remained unclear.

In our system, the nonlinearity originates from the tunnel-coupled wires at the entrance and exit of the electronic Mach-Zehnder interferometer. This is evidenced by experimental measurements of its nonlinear I - V curve and further corroborated by numerical simulations. To illustrate the device's nonlinearity, we decompose the output current into its symmetric, $I^S(V, B) = (I(V, B) + I(-V, B))/2$, and antisymmetric, $I^A(V, B) = (I(V, B) - I(-V, B))/2$, components. The symmetric current is indeed non-zero, as shown in the vertical line cut of the right panel in Fig. 2a, with nonlinearities appearing for bias voltages as low as $25 \mu\text{V}$. In contrast, the antisymmetric current is dominated by a linear response, as seen in the vertical line cut of the right panel in Fig. 2b. To further emphasize the contribution of the nonlinearity towards the coherent oscillations, we analyze the magnetic field dependence. For the symmetric current, AB oscillations with minimal background current are observed (horizontal line cut of the bottom panel in Fig. 2a). On the contrary, the antisymmetric current shows AB oscillations superimposed on a significant background current (horizontal line cut of the bottom panel in Fig. 2b). These oscillations are the characteristic AB oscillations measured in a linear system. To further confirm that the nonlinearity primarily originates from the tunnel-coupled wires, we conducted a separate investigation focusing exclusively on this component of our MZI. We observed a similar nonlinearity to that seen in the entire MZI, reinforcing our hypothesis (for details see Supplementary Information, Section 1.6).

Our experimental findings are supported by state-of-the-art quantum transport simulations (Fig. 2c, d). These simulations combine detailed electrostatic potential simulations³⁰ with transport calculations using the Kwant software^{31,32}. The electrostatic calculations account for the precise geometric configurations of the surface gates and the properties of the GaAs/AlGaAs heterostructure (see

Supplementary Information, Section 2.1 for details). While the simulations reproduce the main features of our measurements in a semi-quantitative manner, some discrepancies persist. These differences likely arise from the simulations not accounting for disorder in the electrostatic potential caused by dopants or for decoherence phenomena. Nonetheless, our simulations indicate that the observed nonlinearity—and the resulting rectification in our system—originates from the energy-dependent transmission of the tunnel-coupled wires (see Supplementary Information, Fig. S8 for details).

Frequency response of the MZI

Having characterised our electronic MZI in the DC regime we now investigate the response of our device under sinusoidal drive at variable frequencies. At low frequencies, the sinusoidal signal is slow enough and the system adjusts instantaneously to the external drive—known as the adiabatic regime. In Fig. 3b, d, we show the amplitude of the coherent current oscillations, I_{AB} , defined as the maximum amplitude of $I_0 - I_1$, extracted from the fast Fourier transform, as a function of frequency and drive amplitude V_{ac} . We observe that for frequencies below 100 MHz, the coherent oscillations are independent of frequency and show the same evolution as a function of drive amplitude. To show that the frequency response at low frequencies (≤ 100 MHz) can be described in the adiabatic limit, we reconstruct the oscillating component I_{AB} , generated by a sinusoidal signal directly from the raw DC data, using the following formula

$$I_{\text{sin}}(V, B) = \frac{1}{T} \int I_{\text{dc}}(V(t), B) dt \quad (1)$$

where I_{sin} is the DC rectified current induced by a sinusoidal drive $V(t) = V_{\text{ac}} \sin(\omega t)$. The evolution of the amplitude of the coherent oscillations I_{AB} passes through a maximum and saturates at high bias. The overall shape of the evolution is well captured by the DC reconstruction (gray continuous line in Fig. 3b), as well as by the Floquet simulations (see Supplementary Information, Section 2.4). In these simulations, the exact position of the maximum with respect to the bias voltage depends on the microscopic parameters of the device. We observe that all experimental data at low frequency (≤ 100 MHz) follow the adiabatic limit.

We now investigate the frequency response of our electronic MZI under sinusoidal drive at frequencies above 100 MHz as shown in Fig. 3d. Contrary to the case at low frequency, as we increase the frequency, a distinct deviation from the adiabatic regime is observed, manifesting itself at frequencies around 1 GHz. This is further supported by our Floquet simulations, which show a similar evolution towards the non-adiabatic regime at similar frequencies as the ones observed in the experiment (see Supplementary Information Section 2.4). These simulations are based on Floquet scattering theory³³, which describes electron transport under periodic voltage drives. Under a time-dependent voltage $V(t)$, electrons acquire a time-dependent phase $\phi(t) = \frac{e}{\hbar} \int V(t) dt$. The Fourier components of the phase factor $e^{-i\phi(t)}$ yield the photo-assisted probabilities P_n , where $n > 0$ ($n < 0$) corresponds to the absorption (emission) of n photons. These probabilities determine the AC transport properties and are used to calculate the rectified current in the system. Our Floquet simulations capture key features of both adiabatic and non-adiabatic regimes, including the emergence of a maximum as a function of voltage bias and deviations from adiabaticity at experimentally relevant frequencies. However, the peak position of coherent oscillations shifts oppositely to experimental observations (see Supplementary Information, Section 2.4), with additional discrepancies at high bias. These differences stem from the limitations of the Floquet scattering approach, which, while capturing essential physics, omits certain effects. In our model, electron-electron interactions are included at the mean-field level in a static way, enabling direct comparison with

Experiments

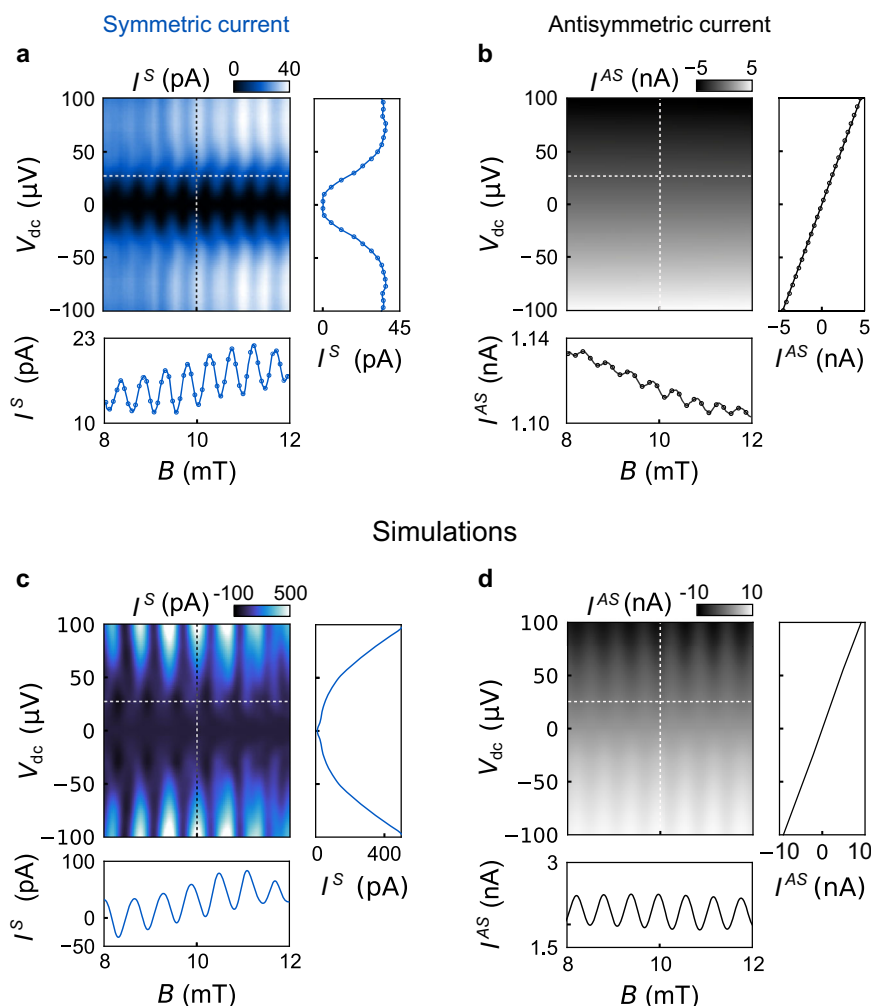


Fig. 2 | Nonlinearity of the electronic Mach-Zehnder interferometer. The DC I - V curve is decomposed into its symmetric (I^S) and antisymmetric (I^{AS}) components with respect to the bias voltage V_{dc} . **a** Density plot of the symmetric component of the current as a function of the DC bias voltage V_{dc} and magnetic field B . The vertical line cut, shows the nonlinear I - V characteristic at a magnetic field of $B = 10$ mT. The horizontal line cut shows AB oscillations at a bias voltage of $V_{dc} = 25$ μV. **b** Same as

(a), but for the antisymmetric component of the current. The I - V characteristic exhibits primarily a linear behaviour. The applied bias voltage is corrected to account for the effective reduction of the bias due to the electronic circuit (Supplementary Information, Section 1.1). **c**, **d** Quantum transport simulations of both the symmetric and antisymmetric components of the current, analogous to (a, b).

experiments without fitting parameters. However, this approach excludes some complex mechanisms. A more advanced treatment—time-dependent Hartree-Fock—has shown that interactions primarily renormalize plasmon velocity while maintaining coherence^{16,34}. Fully accounting for decoherence would require accounting for the dynamical creation of electron-hole pairs which would require to treat higher-order Feynman diagrams, a challenge at the forefront of current research. We expect electron-electron interactions to be the dominant decoherence mechanism³⁵, as observed in DC interferometry³⁶.

To further highlight the frequency-dependent evolution of the oscillation amplitude, we define $\Delta I_{AB}(f)$ as the absolute difference between the maximum oscillation amplitude measured at a given drive frequency f and the maximum oscillation amplitude in the adiabatic limit:

$$\Delta I_{AB}(f) = |\max[I_{AB}(f \rightarrow 0, V_{ac})] - \max[I_{AB}(f, V_{ac})]| \quad (2)$$

This quantity is plotted in Fig. 3e. At low frequencies, the quantum oscillations follow the adiabatic limit up to roughly 1 GHz. Beyond this

frequency, the system presents deviations from the adiabatic limit and gradually evolves towards the non-adiabatic regime.

Notably, accessing the non-adiabatic regime has remained elusive until now, as it was expected to occur at frequencies well above 1 GHz²⁴. We demonstrate, that in our device, this regime is reached at surprisingly low frequencies due to the specific properties of the TCW's conduction modes. Using realistic electrostatic potential simulations, as pioneered in³⁰ (Supplementary Information, Section 2.4), we show that the modes near the Fermi energy exhibit strong energy dependence, leading to nonlinear transport and, consequently, a rectified current. Owing to their low kinetic energy, these modes dominate the frequency response of our device, causing deviations from the adiabatic regime even at frequencies around 1 GHz.

Electronic interference with on-demand single-electron wavepackets

We now demonstrate quantum interference beyond the adiabatic regime with ultrashort wavepackets having a temporal width as short as 30 ps and containing as few as one electron. It is important to emphasize that, in our case, the generated wavepackets are plasmonic

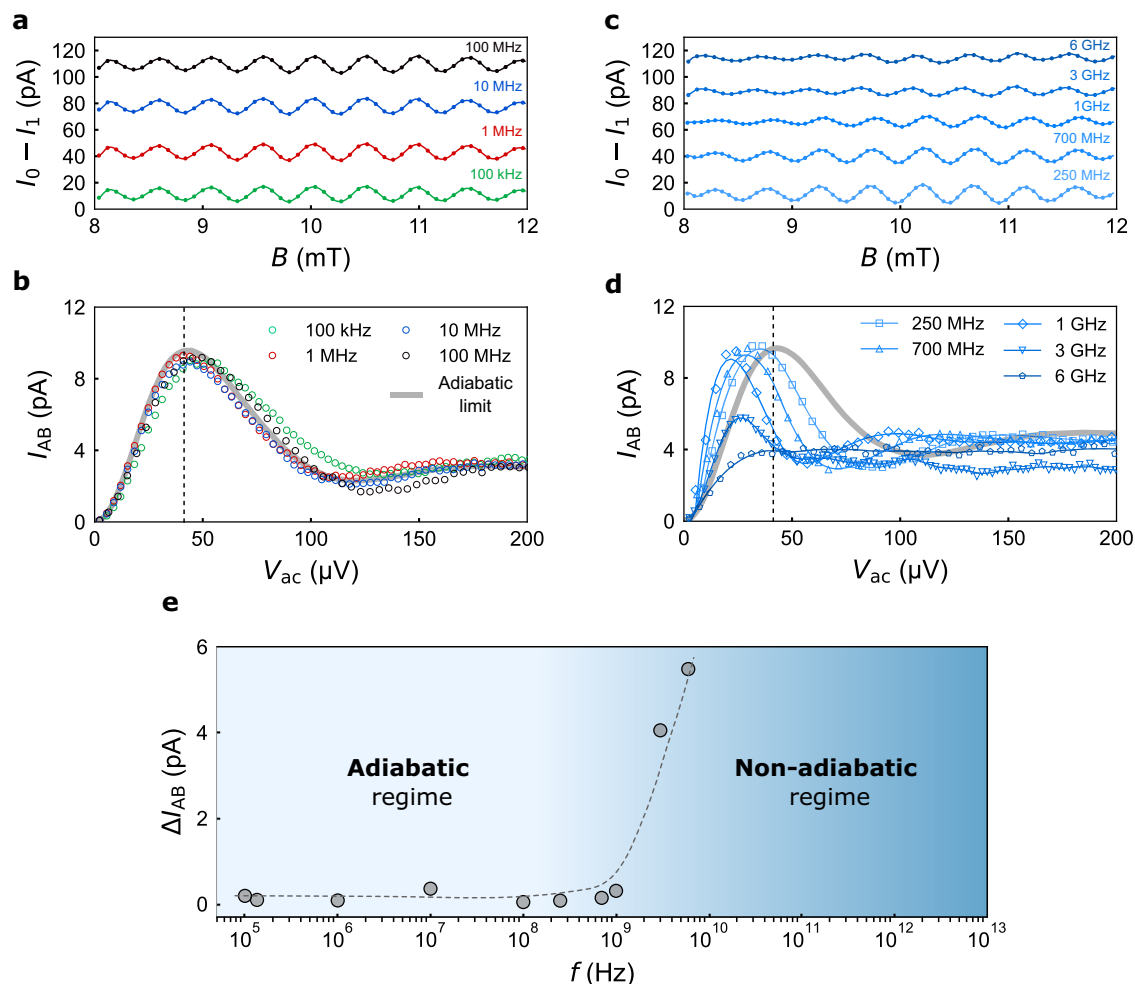


Fig. 3 | Frequency response of the MZI under sinusoidal drive. **a, c** AB oscillations of the current difference $I_0 - I_1$ for frequencies ranging from 100 kHz to 6 GHz. Experimental data are vertically offset for clarity. **b** Amplitude of the AB oscillations I_{AB} versus sinusoidal drive amplitude V_{ac} for frequencies from 100 kHz to 100 MHz. The thick gray line indicates the adiabatic limit calculated from the DC raw data using Eq. 1. **d** Same as **(b)** for frequencies ranging from 250 MHz to 6 GHz. The

adiabatic limit (thick gray line) is shown for comparison. **e** Evolution of the relative amplitude change ΔI_{AB} with frequency calculated using Eq. (2). The dashed line serves as a guide to the eye. Below 1 GHz, ΔI_{AB} remains small, indicating adiabatic behavior. Above 1 GHz, ΔI_{AB} deviates from the adiabatic limit, marking the transition to the non-adiabatic regime.

pulses influenced by electron interactions¹⁶. To begin, we characterise these ultrashort plasmonic wavepackets on-chip using a pump-probe technique^{37,38}. We apply a voltage pulse with a duration of 25 ps³⁹ to the injection Ohmic contact via the AC port of a high-bandwidth bias tee. By applying a second short voltage pulse to the quantum point contact, highlighted in white in Fig. 1a, with a precisely controlled time delay, we can measure the time-resolved trace of the plasmonic wavepacket directly on chip. Time traces for various pulse amplitudes, shown in Fig. 4a, reveal plasmonic pulses with a temporal duration of 30 ps. For such short pulses, we observe quantum oscillations in the output currents of our Mach-Zehnder interferometer device, which are perfectly anti-phased (see Fig. 4b). These interference patterns exhibit minimal background current and remain highly robust under applied bias voltages of up to several hundred microvolts.

To demonstrate that quantum interference can be observed with the on-demand injection of a single electron—a key requirement for realizing a flying electron qubit—we analyse our results in terms of the number of injected and transmitted electrons. We convert the amplitude of the coherent oscillations I_{AB} , as defined above, into the average number of interfering charges n_{AB} using the relation $I = enf$, where e is the electron charge, n is the average number of charges, and $f = 100$ MHz is the pulse repetition frequency. Similarly, we convert the pulse

amplitude V_p into an effective number of injected electrons per pulse n_{inj} (see Supplementary Information, Section 1.5). These results are presented in Fig. 4c for pulses of various temporal widths. We observe that, with ultrashort voltage pulses, it is straightforward to reach a regime where a single electron traverses the interferometer. Remarkably, the contrast of the oscillating signal is significantly enhanced for shorter voltage pulses. This enhancement is primarily attributed to the high-energy components of short plasmonic pulses, which probes a higher energy range of the $I - V$ characteristic and is thus more sensitive to the nonlinearity. A detailed understanding of the enhanced contrast of the coherent oscillations compared to the DC regime is currently lacking. Achieving this would require a microscopic theory that incorporates electron-electron interactions⁴⁰, which is computationally too costly at present.

Finally, let us comment on the relationship between the size of the plasmon pulse and the dimensions of the interferometer. As demonstrated above, the nonlinearity primarily stems from modes near the Fermi energy in the tunnel-coupled wires, which determine the effective propagation speed of the plasmon pulse. These modes exhibit the slowest Fermi velocity, $v_{TCW} \approx 3 \times 10^4 \text{ ms}^{-1}$ while the plasmon propagates at a speed of $\approx 10^6 \text{ ms}^{-1}$ in the interferometer arms. Assuming these velocities for the two different sections of the MZI, the resulting

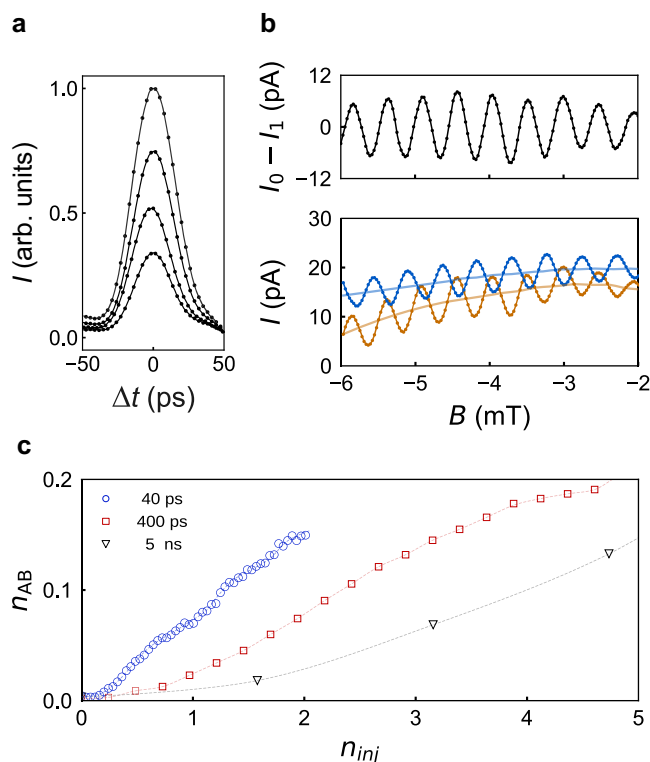


Fig. 4 | Quantum interference with on-demand single-electron plasmonic pulses. **a** Time-resolved measurements of a plasmonic pulse of width $\tau_p = 30$ ps. The envelope is measured in a pump-and-probe experiment by varying the pulse amplitude. **b** Bottom panel shows raw data of Aharonov-Bohm oscillations for the shortest pulse for an amplitude of 100 μ V. Top panel shows the total oscillating current $I_0 - I_1$, where a smooth background has been subtracted. **c** Average number of transmitted charges n_{AB} that contribute to the quantum coherence as a function of injected charges n_{inj} , with pulses of temporal widths τ_p varying from 40 ps to 5 ns. $n_{AB} = n_0 - n_1$ corresponds to the total number of transmitted charges from the upper and lower electron waveguide that contribute to the quantum coherence. The dashed lines are guides to the eye.

total propagation time is calculated to be 144 ps. This timescale corresponds to half the period of a sine wave with a frequency of 3.5 GHz, matching well the frequency range where deviations from the adiabatic regime are observed. These insights suggest that the plasmon wavepacket is significantly smaller than the quantum device, supporting the consistency of our observations. In conclusion, we have demonstrated electronic quantum interference in a 14-micron-long Mach-Zehnder interferometer using plasmonic pulses containing a single charge. By employing GHz sinusoidal excitation and voltage pulses with durations of several tens of picoseconds, we identified a ‘non-adiabatic’ regime. This achievement represents a significant milestone towards realizing flying electron qubits, where the pulse width must be shorter than the dimensions of the quantum device.

Beyond providing the proof-of-principle demonstration of coherent control for ultrashort electron qubits in semiconducting systems, we expect that our detailed high frequency investigation will stimulate further theoretical and experimental research into the electron dynamics of these systems. To complete the implementation of a fully-fledged flying electron qubit, the integration of single-shot detection is essential. A recent advancement has been achieved in this direction⁴¹. The next crucial milestone is to increase the number of flying qubits that can be accommodated within a single processing unit, enabling the implementation of multiple gate operations during their flight. This can be achieved by further reducing the temporal

width of the plasmonic pulses⁴², potentially reaching durations in the terahertz regime⁴³.

Furthermore, our demonstration of coherence in the non-adiabatic regime opens new possibilities for electron quantum optics experiments. This achievement paves the way for exploring dynamical interference control^{23,44} and provides new avenues for investigating single-electron coherence⁴⁵ and multi-particle interference phenomena in electronic MZIs^{46–48}. The coherent manipulation of ultrashort wavepackets in an electronic MZI also represents a crucial step towards coupling multiple interferometers to study entanglement and test Bell inequalities^{49,50}. Moreover, these short wavepackets offer a pathway to high-fidelity quantum teleportation of single-electron states⁵¹, marking a significant advance toward quantum information processing with flying electrons.

Methods

Sample fabrication

The sample is patterned on a GaAs/AlGaAs heterostructure, forming a two-dimensional electron gas (2DEG) located 145 nm below the surface, with carrier density $n_e = 1.9 \times 10^{11} \text{ cm}^{-2}$ and mobility $\mu_e = 1.8 \times 10^6 \text{ cm}^2/(\text{V} \cdot \text{s})$. The electronic Mach-Zehnder interferometer (MZI) geometry is defined by Ti/Au surface gates patterned using electron beam lithography. Electrical connections to the 2DEG are established through Ohmic contacts formed by the successive deposition of Ni(5 nm)/Ge(140 nm)/Au(280 nm)/Ni(100 nm)/Au(15 nm), followed by annealing under a continuous flow of forming gas (5% H_2 in Ar) at 370 °C for 2 min and 430 °C for 1 min. The injection Ohmic contact area measures $10 \times 10 \mu\text{m}^2$.

High frequency signal injection

The high frequency signal (sinusoidal or pulses) was injected into the MZI through coaxial line with a bandwidth of 40 GHz. It was modulated at 170 Hz and injected into a high bandwidth (40 GHz) bias-tee to control independently the AC and DC components of the signal. The ultrashort voltage pulses used in this experiment were generated using a homemade voltage pulse generator based on frequency comb synthesis³⁹, in conjunction with an arbitrary waveform generator with a sampling rate of 24 GS/s. The time-resolved measurement of the 30 ps pulse confirms the precise injection of ultrashort voltage pulses into the MZI without significant distortion.

Electrostatic and quantum transport simulations

Semi-quantitative quantum transport simulations are performed in two steps. First, the electrostatic potential in the silicon doped heterostructure is calculated by solving the Poisson equation with the commercial solver nextnano⁵². We follow the approach adopted in³⁰. To implement the device geometry, we position metallic gold gates on the surface of GaAs crystal, taking into account the Schottky barrier. Surface charges are added to take into account Fermi-level-pinning. The dopant and the surface charge densities are calibrated in such a way that they reproduce an experimental pinch-off measurement between two metallic surface gates. In a second step, a 2D slice of the electrostatic potential at the 2DEG height is extracted and used to compute the DC current. The Landauer-Büttiker formalism⁵³ is employed, and the calculations are performed using the open-source software Kwant³¹. The lattice constant is set to $a = 5$ nm, and the magnetic field is incorporated using the standard Peierl’s substitution. Additionally, the current under periodic drive is calculated from the DC current using Floquet scattering theory, as described in ref. 24.

Data availability

The experimental data generated in this study have been deposited in the Zenodo database under accession code <https://doi.org/10.5281/zenodo.15040085>.

References

- Kjaergaard, M. et al. Superconducting qubits: Current state of play. *Annu. Rev. Condens. Matter Phys.* **11**, 369–395 (2020).
- Burkard, G. et al. Semiconductor spin qubits. *Rev. Mod. Phys.* **95**, 025003 (2023).
- Slussarenko, S. & Pryde, G. J. Photonic quantum information processing: A concise review. *Appl. Phys. Rev.* **6**, 041303 (2019).
- Romero, J. & Milburn, G. Photonic quantum computing. Preprint at arXiv:2404.03367 (2024).
- Maring, N. et al. A versatile single-photon-based quantum computing platform. *Nat. Photonics* **18**, 603–609 (2024).
- Fève, G. et al. An on-demand coherent single-electron source. *Science* **316**, 1169–1172 (2007).
- Blumenthal, M. D. et al. Gigahertz quantized charge pumping. *Nat. Phys.* **3**, 343–347 (2007).
- Dubois, J. et al. Minimal-excitation states for electron quantum optics using levitons. *Nature* **502**, 659–663 (2013).
- Wang, J. et al. Generation of a single-cycle acoustic pulse: A scalable solution for transport in single-electron circuits. *Phys. Rev. X* **12**, 031035 (2022).
- Wang, J. et al. Coulomb-mediated antibunching of an electron pair surfing on sound. *Nat. Nanotechnol.* **18**, 721–726 (2023).
- Ubbelohde, N. et al. Two electrons interacting at a mesoscopic beam splitter. *Nat. Nanotechnol.* **18**, 733–740 (2023).
- Fletcher, J. D. et al. Time-resolved Coulomb collision of single electrons. *Nat. Nanotechnol.* **18**, 727–732 (2023).
- Bäuerle, C. et al. Coherent control of single electrons: a review of current progress. *Rep. Prog. Phys.* **81**, 056503 (2018).
- Edlbauer, H. et al. Semiconductor-based electron flying qubits: review on recent progress accelerated by numerical modelling. *EPJ Quantum Technol.* **9**, 21 (2022).
- Bocquillon, E. et al. Electron quantum optics in ballistic chiral conductors. *Ann. Phys.* **526**, 1–30 (2014).
- Roussely, G. et al. Unveiling the bosonic nature of an ultrashort few-electron pulse. *Nat. Commun.* **9**, 2811 (2018).
- Levitov, L. S., Lee, H. & Lesovik, G. B. Electron counting statistics and coherent states of electric current. *J. Math. Phys.* **37**, 4845–4866 (1996).
- Ivanov, D., Lee, H. & Levitov, L. Coherent states of alternating current. *Phys. Rev. B* **56**, 6839 (1997).
- Assouline, A. et al. Emission and coherent control of Levitons in graphene. *Science* **382**, 1260–1265 (2023).
- Bartolomei, H. et al. Time-resolved sensing of electromagnetic fields with single-electron interferometry. *Nat. Nanotechnol.*, 41565-025-01888-2 (2025).
- Souquet-Basiège, H. et al. Quantum sensing of time dependent electromagnetic fields with single electron excitations. Preprint at arXiv:2405.05796 (2024).
- Pomaranski, D. et al. Semiconductor circuits for quantum computing with electronic wave packets. Preprint at arXiv:2410.16244 (2024).
- Gaury, B. & Waintal, X. Dynamical control of interference using voltage pulses in the quantum regime. *Nat. Commun.* **5**, 3844 (2014).
- Rossignol, B., Kloss, T., Armagnat, P. & Waintal, X. Toward flying qubit spectroscopy. *Phys. Rev. B* **98**, 205302 (2018).
- Yamamoto, M. et al. Electrical control of a solid-state flying qubit. *Nat. Nanotechnol.* **7**, 247–251 (2012).
- Takada, S. et al. Measurement of the transmission phase of an electron in a quantum two-path interferometer. *Appl. Phys. Lett.* **107**, 063101 (2015).
- Kouwenhoven, L. P. et al. Nonlinear conductance of quantum point contacts. *Phys. Rev. B* **39**, 8040–8043 (1989).
- Angers, L. et al. Magnetic-field asymmetry of mesoscopic dc rectification in Aharonov-Bohm rings. *Phys. Rev. B* **75**, 115309 (2007).
- Leturcq, R. et al. Coherent nonlinear transport in quantum rings. *Phys. E* **35**, 327–331 (2006).
- Chatzikiriakou, E. et al. Unveiling the charge distribution of a GaAs-based nanoelectronic device: A large experimental dataset approach. *Phys. Rev. Res.* **4**, 043163 (2022).
- Groth, C. W., Wimmer, M., Akhmerov, A. R. & Waintal, X. Kwant: a software package for quantum transport. *New. J. Phys.* **16**, 063065 (2014).
- Bautze, T. et al. Theoretical, numerical, and experimental study of a flying qubit electronic interferometer. *Phys. Rev. B* **89**, 125432 (2014).
- Moskalets, M. V. *Scattering Matrix Approach to Non-stationary Quantum Transport*. (Imperial College Press, London, 2011).
- Kloss, T., Weston, J. & Waintal, X. Transient and Sharvin resistances of Luttinger liquids. *Phys. Rev. B* **97**, 165134 (2018).
- Ferraro, D. et al. Real-time decoherence of Landau and Levitov quasiparticles in quantum Hall edge channels. *Phys. Rev. Lett.* **113**, 166403 (2014).
- Rouleau, P. et al. Finite bias visibility of the electronic Mach-Zehnder interferometer. *Phys. Rev. B* **76**, 161309 (2007).
- Hashisaka, M. et al. Waveform measurement of charge- and spin-density wave packets in a chiral Tomonaga-Luttinger liquid. *Nat. Phys.* **13**, 559–562 (2017).
- Kamata, H. et al. Fractionalized wave packets from an artificial Tomonaga-Luttinger liquid. *Nat. Nanotechnol.* **9**, 177–181 (2014).
- Aluffi, M. et al. Ultrashort electron wave packets via frequency-comb synthesis. *Phys. Rev. Appl.* **20**, 034005 (2023).
- Safi, I. Driven quantum circuits and conductors: A unifying perturbative approach. *Phys. Rev. B* **99**, 045101 (2019).
- Thiney, V. et al. In-flight detection of few electrons using a singlet-triplet spin qubit. *Phys. Rev. Res.* **4**, 043116 (2022).
- Piccione, N. et al. Reservoir-free decoherence in flying qubits. *Phys. Rev. Lett.* **132**, 220403 (2024).
- Georgiou, G. et al. Efficient three-dimensional photonic-plasmonic photoconductive switches for picosecond THz pulses. *ACS Photonics* **7**, 1444–1451 (2020).
- Gaury, B. et al. Stopping electrons with radio-frequency pulses in the quantum Hall regime. *Phys. Rev. B* **90**, 161305 (2014).
- Haack, G., Moskalets, M., Splettstoesser, J. & Büttiker, M. Coherence of single-electron sources from Mach-Zehnder interferometry. *Phys. Rev. B* **84**, 081303 (2011).
- Hofer, P. P. & Flindt, C. Mach-Zehnder interferometry with periodic voltage pulses. *Phys. Rev. B* **90**, 235416 (2014).
- Rosselló, G., Battista, F., Moskalets, M. & Splettstoesser, J. Interference and multiparticle effects in a Mach-Zehnder interferometer with single-particle sources. *Phys. Rev. B* **91**, 115438 (2015).
- Kotilahti, J. et al. Multi-particle interference in an electronic Mach-Zehnder interferometer. *Entropy* **23**, 736 (2021).
- Bertoni, A. et al. Simulation of entangled electronic states in semiconductor quantum wires. *Phys. B* **314**, 10–14 (2002).
- Vyshnevyy, A. A., Lebedev, A. V., Lesovik, G. B. & Blatter, G. Two-particle entanglement in capacitively coupled Mach-Zehnder interferometers. *Phys. Rev. B* **87**, 165302 (2013).
- Olofsson, E. et al. Quantum teleportation of single-electron states. *Phys. Rev. B* **101**, 195403 (2020).
- Birner, S. et al. nextnano: General purpose 3-D simulations. *IEEE Trans. Electron. Devices* **54**, 2137–2142 (2007).
- Datta, S. *Quantum Transport: Atom to Transistor*. (Cambridge University Press, Cambridge, UK, 2005).

Acknowledgements

We acknowledge fruitful discussions with P. Degiovanni during the preparation of this manuscript. This project has received funding from the European Union H2020 research and innovation program under grant agreement No. 862683, “UltraFastNano”. C.B. acknowledges

funding from the French Agence Nationale de la Recherche (ANR), project ANR QCONTROL ANR-18-JSTQ-0001. C.B., H.S., X.W. and J.S. acknowledge funding from the Agence Nationale de la Recherche under the France 2030 programme, reference ANR-22-PETQ-0012. J.W. acknowledges the European Union H2020 research and innovation program under the Marie Skłodowska-Curie grant agreement No. 754303. M.A. acknowledges the MSCA co-fund QuanG Grant No. 101081458, funded by the European Union and the program QuanTEdu-France n° ANR-22-CMAS-0001 France 2030. L.M. acknowledges the program QuanTEdu-France n° ANR-22-CMAS-0001 France 2030. T.V. acknowledges funding from the French Laboratory of Excellence project “LANEF” (ANR-10-LABX-0051). M.Y. and N-H.K. acknowledge CREST-JST (grant number JPMJCR1876). M.Y. acknowledges JST Moonshot (grant number JPMJMS226B-4). M.Y., D.P., and S.T. acknowledge Japan Society for the Promotion of Science, Grant-in-Aid for Scientific Research S (grant number JP24H00047). S.T. acknowledge CREST-JST (grant number JPMJCR1876) and JST Moonshot (grant numbers JPMJMS226B). G.G. acknowledges EPSRC “QUANTERAN” (grant number EP/X013456/1) and Royal Society of Edinburgh “TEQNO” (grant number 3946). A.D.W. and A.L. thank the DFG via ML4Q EXC 2004/1—390534769, the BMBF-QR.X Project 16KISQ009 and the DFH/UFA Project CDF A-05-06. The present work has been done in the framework of the International Research Project “Flying Electron Qubits”—“IRP FLEQ”—CNRS—Riken—AIST—Osaka University.

Views and opinions expressed are those of the author(s) only and do not necessarily reflect those of the European Union or the granting authority. Neither the European Union nor the granting authority can be held responsible for them.

Author contributions

S.O. fabricated the sample with help from G.G. and performed the experiment with support from M.A., T.V., H.E. and J.W. and technical assistance from C.G., J.S. and M.U. L.M. and T.K. performed the numerical simulations with help from X.W. M.Y., D.P., S.T. and N-H. K. helped in the interpretation of the experimental data. G.G. has participated in the early stage of the project. A.L. and A.D.W. provided the high-quality GaAs/GaAlAs heterostructure. S.O., L.M. and T.K. wrote the manuscript with feedback from all authors. H.S. and C.B. supervised the experimental work. C.B. has initiated the project.

Competing interests

The authors declare no competing interests.

Additional information

Supplementary information The online version contains supplementary material available at <https://doi.org/10.1038/s41467-025-58939-4>.

Correspondence and requests for materials should be addressed to Christopher Bäuerle.

Peer review information : *Nature Communications* thanks the anonymous reviewers for their contribution to the peer review of this work. A peer review file is available.

Reprints and permissions information is available at <http://www.nature.com/reprints>

Publisher's note Springer Nature remains neutral with regard to jurisdictional claims in published maps and institutional affiliations.

Open Access This article is licensed under a Creative Commons Attribution-NonCommercial-NoDerivatives 4.0 International License, which permits any non-commercial use, sharing, distribution and reproduction in any medium or format, as long as you give appropriate credit to the original author(s) and the source, provide a link to the Creative Commons licence, and indicate if you modified the licensed material. You do not have permission under this licence to share adapted material derived from this article or parts of it. The images or other third party material in this article are included in the article's Creative Commons licence, unless indicated otherwise in a credit line to the material. If material is not included in the article's Creative Commons licence and your intended use is not permitted by statutory regulation or exceeds the permitted use, you will need to obtain permission directly from the copyright holder. To view a copy of this licence, visit <http://creativecommons.org/licenses/by-nc-nd/4.0/>.

© The Author(s) 2025